

Ultrasmall radial polarizer array based on patterned plasmonic nanoslits

Kentaro Iwami, Miho Ishii, Yuzuru Kuramochi, Kenichi Ida, and Norihiro Umeda

Citation: *Appl. Phys. Lett.* **101**, 161119 (2012); doi: 10.1063/1.4761943

View online: <http://dx.doi.org/10.1063/1.4761943>

View Table of Contents: <http://apl.aip.org/resource/1/APPLAB/v101/i16>

Published by the [American Institute of Physics](#).

Related Articles

Localized surface plasmon resonances in highly doped semiconductors nanostructures

Appl. Phys. Lett. **101**, 161113 (2012)

Polarization dependant scattering as a tool to retrieve the buried phase information of surface plasmon polaritons

Appl. Phys. Lett. **101**, 161603 (2012)

Controllable plasmonic antennas with ultra narrow bandwidth based on silver nano-flags

Appl. Phys. Lett. **101**, 153118 (2012)

Resonant plasmonic effects in periodic graphene antidot arrays

Appl. Phys. Lett. **101**, 151119 (2012)

Silver nanoisland enhanced Raman interaction in graphene

Appl. Phys. Lett. **101**, 153113 (2012)

Additional information on *Appl. Phys. Lett.*

Journal Homepage: <http://apl.aip.org/>

Journal Information: http://apl.aip.org/about/about_the_journal

Top downloads: http://apl.aip.org/features/most_downloaded

Information for Authors: <http://apl.aip.org/authors>

ADVERTISEMENT



ACCELERATE COMPUTATIONAL CHEMISTRY BY 5X.
TRY IT ON A FREE, REMOTELY-HOSTED CLUSTER.

[LEARN MORE](#)

Ultrasmall radial polarizer array based on patterned plasmonic nanoslits

Kentaro Iwami,^{a)} Miho Ishii, Yuzuru Kuramochi,^{b)} Kenichi Ida, and Norihiro Umeda

Department of Mechanical Systems Engineering, Tokyo University of Agriculture and Technology, 2-24-16 Nakacho, Koganei, Tokyo 184-8588, Japan

(Received 4 September 2012; accepted 8 October 2012; published online 19 October 2012)

We developed an ultrasmall radial or azimuthal polarization converter of size ranged from 10 to 100 μm . The converter consists of a half-wave plate divided into four quadrants, each of which is made of periodic gold nanoslits at different orientations in steps of 45° . The converter and its array were fabricated and followed by an evaluation with the Sénarmont method and the polarization microscopy. Due to the giant birefringence of the gold nanoslits, each slit segment achieved 180° retardation at the wavelength of 633 nm, and the conversion from linear to radial polarization was demonstrated. © 2012 American Institute of Physics. [<http://dx.doi.org/10.1063/1.4761943>]

Radially and azimuthally polarized lights have attracted much interest because of their unique axially symmetric distribution of the polarization state in a beam cross section, in contrast to the homogeneously polarized beams. These polarizations have been widely studied and applied to many fields, including fine focusing for high resolution optical microscopy,¹ laser machining,² optical manipulation,³ plasmonic focusing,⁴ Raman spectroscopy,⁵ and photothermal therapy.⁶ In particular, the generation of a large longitudinal electric field component is a significant characteristic of focused radially polarized light, and it has opened up unique applications such as particle acceleration.⁷

The generation of these polarizations relies on the local control of both the polarization orientation and phase. Several methods have been studied to accomplish this, including polarization selection at a laser cavity^{8,9} or use of a radial polarization converter (RPC). Of the wide variety of RPCs that have been studied, examples include orientation-tailored liquid crystal (LC),^{10,11} LC-based spatial light modulators (SLMs),¹ spatially varying retardation (SVR) based on optical crystal^{5,12} or photonic crystal,¹³ sub-wavelength grating,¹⁴ and glass nanostructuring.¹⁵

On the other hand, recent advances in microelectromechanical systems (MEMS) have opened up a world of “parallel optics,” represented by micromirror array or microlens array devices, which have been applied in areas from basic science to the telecommunications of the future.^{16,17} The use of radially or azimuthally polarized light in the field of parallel optics may offer many opportunities, for example, high-throughput nanoscale surface imaging, sensing, and modification by combining them with MEMS probe array system. However, such an application has not yet been realized because axially symmetric beams cannot be arranged in parallel. Therefore, a RPC array is critically needed. Conventional RPCs, however, have disadvantages for this purpose. The main obstacle is the difficulty in fabricating microscale RPCs. The size and resolution of SLMs are not MEMS compatible, and the low damage threshold of LC-

based devices restricts their application. SVR plates, which consist of half-wave plate crystal pieces divided into four or eight segments, are difficult to miniaturize. The sub-wavelength gratings formed on dielectric substrates have advantages for micromachining, but the application is limited to the mid-infrared range because the micromachining of optically transparent material with the sub-wavelength resolution is difficult. Although photonic crystals would satisfy the above requirements, its fabrication is difficult because multilayer deposition is essential. Minimum featuring size of glass-nanostructured RPC is still unclear.

Periodic nanoslit arrays on noble metal thin films were utilized to induce giant birefringence, and more than a 180° phase shift was achieved with nanoscale-thickness.¹⁸ This structure is most compatible with miniaturization because it can be fabricated through conventional electron beam (EB) or nano-imprint lithography combined with a lift-off process, as is expected for future mass-produced wave plates.^{18,19} Furthermore, by arranging nanoslit arrays into a pattern, the spatial distribution of polarization can be theoretically tailored. In this paper, we design, develop, and demonstrate an ultrasmall RPC based on a half-wave plate divided into four quadrants that are composed of patterned plasmonic nanoslit arrays.

Figure 1 shows a schematic drawing of a plasmonic RPC and its cross section. As shown in Fig. 1(a), the RPC consists of four segments of a nanoslit array of a gold thin film deposited on a transparent substrate. Each array segment has identical slit width and period. Figure 1(b) shows the orientation of polarization. Since the phase shifts are opposite between the transverse electric (TE: the electric field is parallel to the nanoslits) and the transverse magnetic (TM: the electric field is perpendicular to the nanoslits) polarizations, a giant birefringence can be achieved.¹⁸ As shown in Fig. 1(a), the four segments, or quadrants, are arranged by changing each slit orientation in steps of 45° . In this structure, the TE axis (fast axis) is treated as the principal axis of the slit array because the phase shift for the TE wave is positive, in contrast to the negative phase shift for the TM wave. Therefore, the principal axes of the four quadrants from 1 to 4 can be described as 45° , 90° , 135° , and 0° , respectively. If each quadrant achieves a retardation of 180° , the arrays work as a half-wave plate divided into fourths. Consequently, 45° and

^{a)} Author to whom correspondence should be addressed. Electronic mail: k_iwami@cc.tuat.ac.jp. URL: <http://nmems.lab.tuat.ac.jp/en/>.

^{b)} Present address: Department of Precision Engineering, the University of Tokyo, Tokyo, 113-8656, Japan.

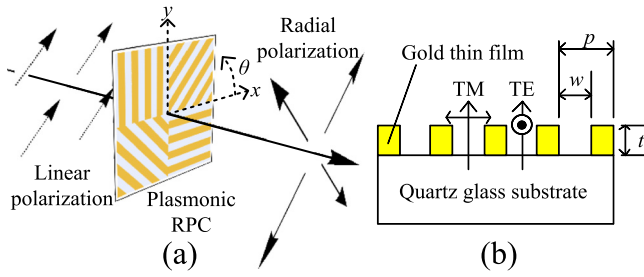


FIG. 1. (a) Schematic drawing of the RPC based on a plasmonic gold nanoslit pattern. It consists of four quadrants, each having 180° retardation. The RPC is arranged by changing the slit orientation in steps of 45°. As the nanoslit array has its principal axis (fast axis) along a slit, a 45° linear-polarized light can be converted to a radially polarized light. (b) Schematic of a cross section of each slit array allocated on each quadrant.

135° linear-polarized incident light can be converted into radially and azimuthally polarized light, respectively.

When developing a plasmonic half-wave plate of metal nanoslits, design parameters should be optimized; however, it is difficult to estimate the phase shift accurately on the basis of analytical waveguide theory. For example, propagation constants for the TE and TM waves are given by,¹⁸

$$k_{TE} = \sqrt{k_0^2 - (\pi/w_{eff})^2}, \quad (1)$$

$$\tanh\left(\frac{w}{2} \sqrt{k_{TM}^2 - k_0^2}\right) = -\frac{\sqrt{k_{TM}^2 - \epsilon_m k_0^2}}{\epsilon_m \sqrt{k_{TM}^2 - k_0^2}}, \quad (2)$$

where k_{TE} and k_{TM} are propagation constants for the TE and TM modes, respectively; and w and w_{eff} are the raw and effective widths of the slit, respectively; and ϵ_m is a dielectric function of the metal. As shown in Eq. (1), k_{TE} has a sharp cutoff at $\lambda = w_{eff}/2$. However, for gold thin films, cutoff is not sharp but gradual around this wavelength.²⁰ Therefore, numerical analysis is essential to the design of a plasmonic nanoslit half-wave plate.

To determine the optimal slit design, a numerical simulation based on commercially available finite-difference time-domain (FDTD) software (RSoft, FULLWAVE 8.1) was performed. As a half-wave plate, identical transmittance between the TE and the TM waves is important for the plasmonic nanoslit array, together with a 180° phase shift. Figure 2(a) shows contour plots of the phase shifts and the ratio of amplitude transmittance (A_{TE}/A_{TM}) for a 500-nm-period slit array under a 633 nm incident wavelength. In Fig. 2(a), the solid and dashed contours correspond to the phase shifts and transmittance ratios, respectively. Since the contours of a 180° phase shift and an identical transmittance ratio intersect at a gold film thickness of 320 nm and a slit width of 240 nm, a plasmonic nanoslit half-wave plate can be developed at this point. Fig. 2(b) shows the regions at which phase shifts can be achieved between 175° and 185° together with transmittance ratios between 0.95 and 1.05 for each incident wavelength on a 500-nm-period gold slit array. As shown in Fig. 2(b), a plasmonic nanoslit half-wave plate can be achieved for a broad range in the visible spectrum. Fig. 2(c) shows amplitude transmittance of above-mentioned regions.

The RPC pattern was defined on a quartz glass substrate of thickness 525 μm through EB lithography. A 5-nm-thick

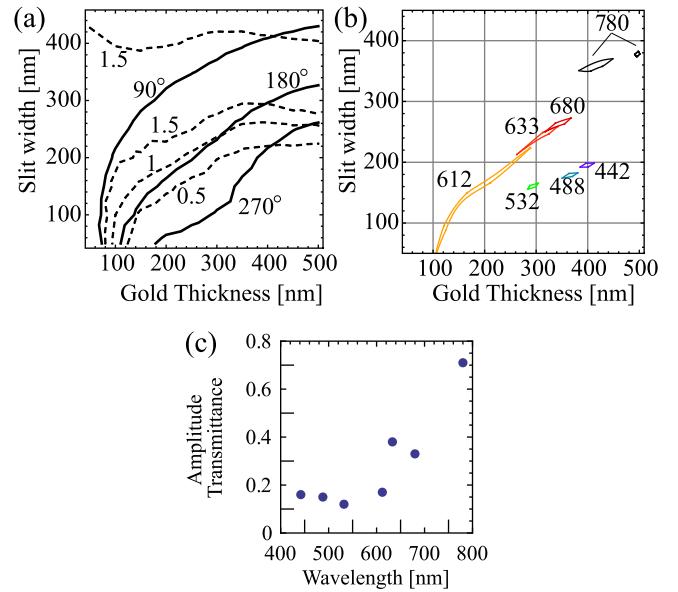


FIG. 2. (a) Contour plots of phase shifts (solid curves) and the ratio of amplitude transmittance (A_{TE}/A_{TM} , dashed curves) for the 633 nm incident wavelength. The pitch of the slit array was fixed to 500 nm. (b) Regions to achieve both 175–185° phase shift and 0.95–1.05 amplitude ratio for each incident wavelength. (c) Amplitude transmittance spectrum of above-mentioned regions.

chromium layer was deposited by the EB deposition for adhesion, followed by the deposition of a gold layer. Next, the EB resists were removed by an organic solvent, and a metal nanoslit pattern was developed (lift-off process). Sizes of single RPC ranged from 10 to 100 μm . Two types of slit arrays were fabricated, one with a slit width of 300 nm and the other, 350 nm with a slit pitch of 525 nm due to lithography limitation. In order to achieve a 180° phase shift at the 300-nm-wide slit, the gold thin film was deposited with a thickness of 445 nm. Fig. 3(a) shows a scanning electron microscopy (SEM) image of the fabricated 3×3 array of the 10 μm RPC array with the slit width of 300 nm.

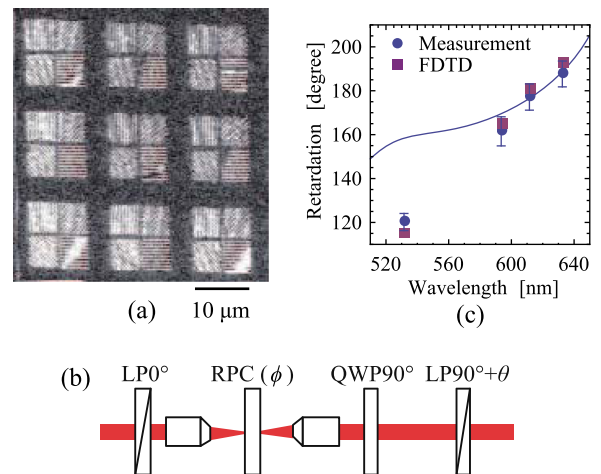


FIG. 3. (a) An SEM image of a fabricated 3×3 RPC array. The size of an RPC unit is 10 μm . (b) Experimental setup for the retardation measurement based on the Sénarmont method. (c) Retardation spectra on 525-nm-period and 300-nm-wide gold nanoslit by Sénarmont method measurement (circle), FDTD calculation (square), and theoretical estimation (solid line), respectively. Error bars indicate standard deviations over four quadrants ($n = 50$ for each quadrant).

TABLE I. Retardation (deg) for 633-nm irradiation of each nanoslit array quadrant with slit widths of 350 and 300 nm. The period and thickness of both slit arrays are 525 and 445 nm, respectively.

Quadrant	Slit width	
	350 nm	300 nm
1	116.3	175.7
2	71.65	184.9
3	147.9	184.7
4	70.24	181.1

The phase shifts of each quadrant were measured by the Sénarmont method. Figure 3(b) shows the experimental setup. A He-Ne laser ($\lambda = 633$ nm) beam passes through a linear polarizer whose transmission axis is 0° (LP 0°), and is focused onto each quadrant. The RPC with the size of $100 \mu\text{m}$ was used. The RPC was rotated with a degree of ϕ to keep the angle between the fast axis of each quadrant at 45° . Therefore, ϕ for the quadrants 1, 2, 3, and 4 were 0° , -45° , -90° , and -135° , respectively. The transmitted beam was collimated by an objective lens and passed through a 90° Babinet-Soleil compensator as a quarter-wave plate (QWP 90°) and a 90° linear polarizer as an analyzer. Finally, the power of the transmitted beam was measured by rotating the analyzer (LP $90^\circ + \theta$).

Table I shows the summary of retardation for RPCs with slit widths of 350 and 300 nm for 633 nm light. For both slits, the slit period was 525 nm. As expected, the 300-nm-slit RPC shows retardation of about 180° for every quadrant. This result confirms that each quadrant of the 300-nm-wide nanoslit array acts as a half-wave plate. In 350-nm-wide slit, the large retardation difference between orthogonal arrangement (quadrants 2 and 4) and diagonal arrangement (quadrants 1 and 3) is observed. It is possibly due to shape error since variable shaped e-beam was used.

Figure 3(c) shows the retardation spectra of a 300-nm-wide slit under laser irradiation at four wavelengths (532, 576, 614, and 633 nm) measured by the Sénarmont method (circle), FDTD calculation (square), and theoretical estimation (solid line), respectively. As shown in Fig. 3(c), theoretical estimation based on Eqs. (1) and (2) does not agree with the other methods in the short wavelength region. In contrast, the FDTD calculation agrees well with the experimental result.

To determine the principal axes of each quadrant, the dependence of the rotation angle on transmitted intensity was measured for the 350-nm-slit RPC, and the results were evaluated by fitting to the theoretical curve of the S_0 component of Stokes vector. In this setup, we assumed each quadrant as an optical retarder with the principal axis of $\phi + 45^\circ$ and a retardation of Δ . For example, the S_0 component of transmitted light through the quadrant 1 ($\phi = 0^\circ$) is expressed as follows:

$$S_0 = \frac{1}{4} \{1 + \cos(\Delta - 2(90^\circ + \theta))\}. \quad (3)$$

Fig. 4 shows the normalized intensity and the fitted S_0 curves for each RPC quadrant. As shown here, all the experi-

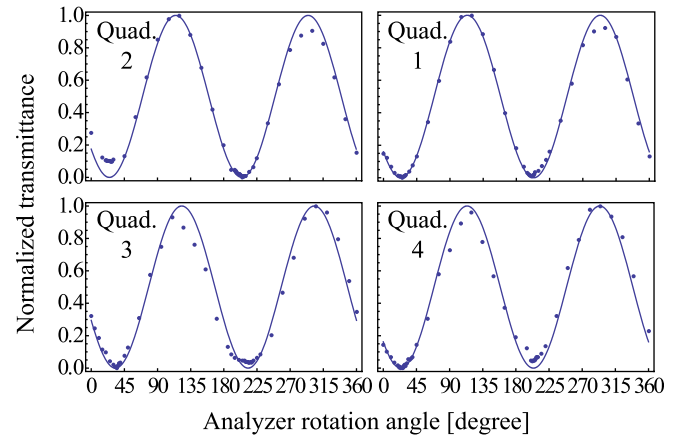


FIG. 4. Normalized intensity of transmitted light through each quadrant of RPC and fitting with S_0 component of Stokes vector.

mental results agree well with the retarder model, and the principal axes of each quadrant are confirmed as the TE direction (parallel to the slit). Therefore, it is confirmed that the fabricated nanoslit array pattern can act as four-quadrant half-wave plates, that is, an RPC.

To demonstrate the fabricated RPC visually, a polarization microscope was used to observe it. Fig. 5 shows optical microscope images under polarized illumination with and without an optical bandpass filter at 633 nm. As illustrated in Fig. 5, a 45° input linear polarization should be converted into radial polarization by the RPC. The transmitted light is imaged by a charge-coupled device (CCD) camera through an analyzer with the transmission axis at 45° (upper images) and 135° (lower images), with and without the 633-nm optical bandpass filter. As shown in the images with the 633 nm filter, the RPC pattern exhibits the expected contrast; the quadrants 1 and 3 are bright with the 45° analyzer, and the quadrants 2 and 4 are bright with the 135° analyzer. In contrast, the white light images do not show clear RPC-like response because of the wavelength-dependent retardations from the nanoslit. The differences in brightness between kitty-cornered quadrants obtained with 633 nm filters can be attributed to the differences of transmittance between the TE and the TM polarizations resulting from the fabrication fluctuation in slit dimensions. Intra-quadrant inhomogeneity of transmittance is also obtained, the reason can be due to partial peeling or sticking occurred during the development procedure of EB resist.

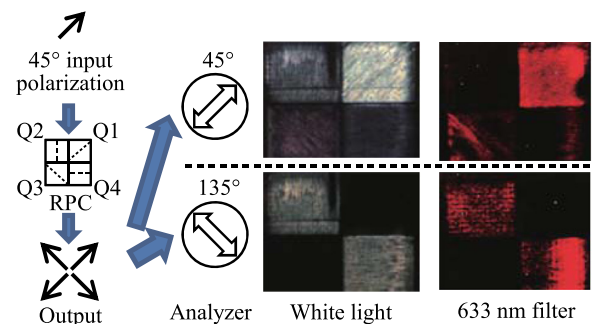


FIG. 5. Polarization microscope images of the 300-nm-wide slit RPC illuminated by white light with and without a 633 nm bandpass filter. Dashed lines at RPC symbol indicate fast axes of quadrants (slit direction). Symbols Q1-Q4 indicate the number of each quadrant.

In conclusion, a radial polarization converter that made use of a gold nanoslit pattern was designed and fabricated on a glass substrate. The size of the RPC ranged from 10 to 100 μm in length and was 445 nm in thickness. With proper slit width and gold thickness design, the RPC will be useful in a large portion of the visible spectrum ranged 442 to 780 nm. Improvement of the low transmittance of nanoslit is the further challenge to a practical device, which will be achieved by optimizing slit pitch, modifying pattern from slit to for example rectangle,²¹ or possibly adopting a technique of electromagnetically induced transparency.²² We are expecting to broaden the usefulness to the ultraviolet region by changing the plasmonic material from gold to silver or aluminum.

The authors would like to thank the Grant-in-Aid for Young Researchers (A) No. 23686016 from the Japanese Society for the Promotion of Science (JSPS) for financially supporting this research. A part of this research was supported by the “Nanotechnology Network” of the Ministry of Education, Culture, Sports, Science and Technology (MEXT), Japan for electron beam lithography at Toyota Technological Institute and VLSI Design and Education Center (VDEC), the University of Tokyo.

¹T. Wilson, F. Massoumian, and R. Juskaitis, *Opt. Eng.* **42**, 3088 (2003).

²V. G. Niziev and A. V. Nesterov, *J. Phys. D: Appl. Phys.* **32**, 1455 (1999).

³Q. Zhan, *Opt. Express* **12**, 3377 (2004).

⁴W. Chen, D. C. Abeyasinghe, R. L. Nelson, and Q. Zhan, *Nano Lett.* **9**, 4320 (2009).

⁵Y. Saito, N. Hayazawa, H. Kataura, T. Murakami, K. Tsukagoshi, Y. Inouye, and S. Kawata, *Chem. Phys. Lett.* **410**, 136 (2005).

⁶H. Kang, B. Jia, J. Li, D. Morrish, and M. Gu, *Appl. Phys. Lett.* **96**, 063702 (2010).

⁷Y. Liu, D. Cline, and P. He, *Nucl. Instrum. Methods Phys. Res. A* **424**, 296 (1999).

⁸A. Nesterov and V. Niziev, *J. Phys. D: Appl. Phys.* **32**, 2871 (1999).

⁹L. Cai, J. Zhang, W. Bai, Q. Wang, X. Wei, and G. Song, *Appl. Phys. Lett.* **97**, 201101 (2010).

¹⁰H. Ren, Y.-H. Lin, and S.-T. Wu, *Appl. Phys. Lett.* **89**, 051114 (2006).

¹¹I. Nishiyama, N. Yoshida, Y. Otani, and N. Umeda, *Meas. Sci. Technol.* **18**, 1673 (2007).

¹²G. Machavariani, Y. Lumer, I. Moshe, A. Meir, and S. Jackel, *Opt. Commun.* **281**, 732 (2008).

¹³H. Kawauchi, Y. Kozawa, S. Sato, T. Sato, and S. Kawakami, *Opt. Lett.* **33**, 399 (2008).

¹⁴Z. Bomzon, G. Biener, V. Kleiner, and E. Hasman, *Opt. Lett.* **27**, 285 (2002).

¹⁵M. Beresna, M. Gecevičius, P. G. Kazansky, and T. Gertus, *Appl. Phys. Lett.* **98**, 201101 (2011).

¹⁶S. Singh-Gasson, R. D. Green, Y. Yue, C. Nelson, F. Blattner, M. R. Sussman, and F. Cerrina, *Nat. Biotechnol.* **17**, 974 (1999).

¹⁷L. Schares, D. M. Kuchta, and A. F. Benner, in *2010 18th IEEE Symposium on High Performance Interconnects* (IEEE, 2010), pp. 104–108.

¹⁸S.-Y. Hsu, K.-L. Lee, E.-H. Lin, M.-C. Lee, and P.-K. Wei, *Appl. Phys. Lett.* **95**, 013105 (2009).

¹⁹P. F. Chimento, N. V. Kuzmin, J. Bosman, P. F. A. Alkemade, G. W. 't Hoof, and E. R. Eliel, *Opt. Express* **19**, 24219 (2011).

²⁰M. Shcherbakov, M. Dobynde, T. Dolgova, D.-P. Tsai, and A. Fedyanin, *Phys. Rev. B* **82**, 193402 (2010).

²¹H. Li, X. Luo, Z. Guo, K. Wen, and L. Yan, *Mod. Phys. Lett. B* **26**, 1250070 (2012).

²²N. Liu, L. Langguth, T. Weiss, J. Kästel, M. Fleischhauer, T. Pfau, and H. Giessen, *Nature Mater.* **8**, 758 (2009).